

Effect of Sn additions on the microstructure, mechanical properties, corrosion and bioactivity behaviour of biomedical Ti–Ta shape memory alloys

Mustafa K. Ibrahim¹ · E. Hamzah¹ · Safaa N. Saud² · E. M. Nazim¹ · N. Iqbal^{3,4} · A. Bahador¹

Received: 28 January 2017 / Accepted: 12 August 2017 / Published online: 30 August 2017
© Akadémiai Kiadó, Budapest, Hungary 2017

Abstract Ti–Ta and Ti–Ta–xSn shape memory alloys (SMAs) were produced successfully by microwave sintering. Tin element was added to Ti–Ta SMA with three different atomic percentages (0.37, 0.745 and 2.26 at.%). The influences of Sn addition on microstructure, transformation temperatures, mechanical properties, shape memory behaviours, corrosion resistance and bioactivity were investigated. It was found that the morphologies of the modified and unmodified Ti–Ta alloys contain a plate-like and needle-like structure, where the former structure is related to the β phase and the latter related to the α phase. The transformation temperatures of M_s to M_f with and without Sn additions were observed to be in the range of 389.65 to 355 K, while the transformation temperatures of A_s to A_f were found to be in the range of 250.42 to 365.8 K. By increasing the proportion of Sn, the compressive fracture strength and shape memory behaviour were enhanced; however, the corrosion resistance tended to be decreased. Based on the bioactivity results, antibacterial activity was improved with the addition of Sn. In conclusion, the existent results indicate that Ti–30 at.% Ta SMAs may be a

convenient alternative to Ni–Ti for certain biomedical applications.

Keywords Porous Ti–30Ta–xSn SMAS · Microwave sintering · Microstructure · Mechanical properties and corrosion · Bioactivity

Introduction

Shape memory alloys (SMAs) have a unique combination of several important properties, including shape memory effect (SME), superelasticity (SE) or pseudoelasticity (PE) and high damping capacity [1, 2]. Titanium-based alloys have been widely used for body implants, such as medical devices, hip joints and dental implants because of their robust ductility, excellent corrosion resistance and high yield strength [3, 4]. In many engineering applications, Ti–Ni alloys have attracted much interest based on their potential utility as functional materials, such as in active, smart structure or adaptive and certain biomedical applications [5–7]. Ti–Ni alloys have several unique features, from their biological performance to physical and chemical properties, rendering them appropriate for employment in universal biomedical scenarios [8, 9] because of their unique superelasticity [10], excellent shape memory effect [11], low elastic modulus [12], superb corrosion resistance and biocompatibility [13–16] and non-ferromagnetic attributes [17]. Recently, the toxicity and hypersensitivity of Ni has been seen to have an effect on the development of Ni-free shape memory alloys [18]. However, the toxicity of Ni forces the usage of non-toxic biocompatible elements, such as Nb and Ta [19–21]. It is known that certain β -Ti alloys exhibit SE as well as SME [22], as apparent in TiNb [23, 24], TiMo [25, 26], TiV [27] and TiTa-based alloys

✉ E. Hamzah
esah@fkm.utm.my

¹ Faculty of Mechanical Engineering, Universiti Teknologi Malaysia, 81310 UTM Johor Bahru, Johor, Malaysia

² Faculty of Information Sciences and Engineering, Management and Science University, Shah Alam, Selangor, Malaysia

³ Medical Devices and Technology Group (MEDITEG), Faculty of Biosciences and Medical Engineering, Universiti Teknologi Malaysia, 81310 Johor Bahru, Johor, Malaysia

⁴ Department of Biomedical Engineering, University of Engineering and Technology, KSK Campus, GT Road, Lahore, Pakistan

[28]. However, TiNb alloys have too low a critical stress for a slip, making it difficult to obtain favourable SME. TiMo alloys are liable to ω -phase embrittlement, and the cytotoxicity of vanadium may mean that TiV alloys are not suitable for biomedical materials [28]. Ti–Ta alloys possess great potential for biomedical applications as a result of their SME, corrosion resistance and low modulus [29–32]. As well, the SME of Ti–Ta alloys can be improved by alloying and with thermo-mechanical treatment [29, 33, 34]. The increase in the relative content of Ta in a Ti matrix causes a decrease in the martensitic transformation temperature (M_s) [28]. Therefore, incorporation of numerous ternary elements into β -type titanium alloys reveals that Sn stabilizes the SME. Sn hampers the formation of the ω -phase and the associated stabilization of the parent β phase [33, 35, 36]. It was reported that the corrosion behaviour of Ti–Ta alloys is enhanced via adding Sn [34, 37, 38], while the effect of this element on antibacterial properties is superior because of the presence of tin oxides that further enriches these properties [39, 40]. However, the improvement in mechanical properties, like shape memory and ductility, is affected by controlling pore size, pore shape, pore distribution, grain size, structure, precipitate formations, morphology of the existing phases and a degree of order. Therefore, the aim of this research was to investigate the influences of various additions of Sn on the microstructure characteristics, mechanical properties, corrosion and bioactivity behaviour of Ti–Ta SMAs. The obtained results will be beneficial for the development of Ti–Ta SMAs for biomedical applications.

Materials and methods

In this work, the elemental powders of Ti and Ta with Sn as an additional element were prepared through a powder metallurgy process. The specification of the elemental powder, composition and ball milling parameters are presented in Table 1. These powders of Ti–30Ta– x Sn SMAs (x is 0, 0.37, 0.745 and 2.26 at.%) were prepared by mechanical alloying using a planetary ball mill (PM100). The mixed powders were cold-pressed to green samples of $\Phi 25 \times 10$ mm under a uniaxial pressure of 230 kg cm⁻²

for 5 min, followed by microwave sintering (HAMiLab-V3, SYNOTHERM Corp.). Specifically, the green samples were microwave sintered at a temperature of 1173 K for 30 min at a heating rate of 303 K min⁻¹. Figure 1 is a schematic diagram of the MWS vacuum pot containing the insulation barrel that was set up continuously at 2.45 GHz and 4.5 kV. The sintering was performed under an argon gas atmosphere that filled the sintering chamber with gas flow purity of 99.999%. The green samples were placed in an alumina crucible surrounded by silicon carbide (SiC) particles (at the corners of the alumina crucible). SiC was used as an auxiliary heat material. An infrared pyrometer employed to measure the temperature of the samples during sintering.

The sintered samples were cut into 7 mm \times 7 mm \times 14 mm dimensions by using an electrical discharge machining (EDM) wire cutter for compression testing based on ASTM E9-09 and dimensions of 10 mm \times 10 mm \times 20 mm for shape memory testing. The corrosion test was performed with $\Phi 13.5 \times 2$ mm samples, while the sample dimensions for the antibacterial test were $\Phi 5 \times 1.5$ mm.

Scanning electron microscopy (SEM, Hitachi Model S-3400 N) was utilized to analyse microstructure. The Archimedes drainage method was employed to determine the porosity of the sintered samples. The phase and crystal structure were identified using a D5000 Siemens X-ray diffractometer fitted with a Cu K α X-ray source in a locked-coupled mode, a 2θ range between 20° and 90° and a 0.05° s⁻¹ scanning step. Differential scanning calorimetry (DSC Q200, TA Instrument) was used to identify the phase transformation temperatures of these alloys with the TA Instrument software at heating/cooling rates of 283 K min⁻¹. The compression test was performed with an Instron 600 DX-type universal testing machine at a constant speed of 0.5 mm/min at room temperature. Vickers hardness (Matsuzawa–Vicker type) was employed under a force of 30 kg for 20 s for a hardness test determined at room temperature. The SME test was carried out using an Instron 600 DX-type universal testing machine, which operated with special program parameters based on the SME test. The loading–unloading cycle compressive test was performed at a strain of 4% and a temperature of

Table 1 Specification of elemental powders and mixtures

Element	Powder specification			Ball milling parameters		
	Purity/%	Size/ μ m	Composition/at.%	Rotation speed/rpm	Ball-to-powder ratio	Time/h
Ti	99.5	150	70	300	4:1	1
Ta	99.9	45–150	30			
Sn	99.5	45	0.37, 0.745 and 2.26			

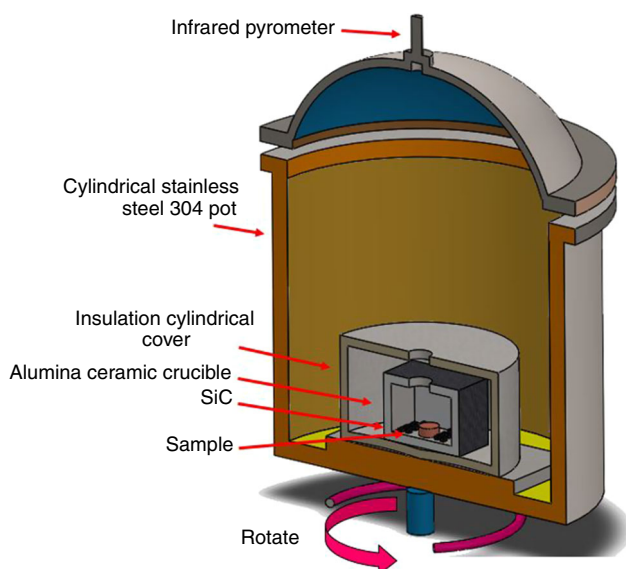


Fig. 1 Schematic diagram of MWS vacuum pot containing the insulation barrel

310 K (human body temperature), below martensite start temperature (M_s) to obtain shape recovery followed by heating at 473 K for 30 min [above austenite finish temperature (A_f)] and water quenching. To evaluate the corrosion behaviour of Ti–Ta– x Sn (x is 0, 0.37, 0.745 and 2.26 at.%) SMAs, a potentiodynamic polarization (PDP) was carried out in simulated body fluid (SBF). The specimens were connected to an open-air glass cell with a surface area of 0.2 cm², where the open-air glass cell contained approximately 300 mL SBF of pH (7.4), and the experiment was accomplished at human body temperature (310 K) with a scan rate of 2 mV s⁻¹ at -250 mV. The VersaSTAT 3 machine was utilized to record the measured data, and three-electrode cells were attached to this equipment: (1) the saturated calomel electrode (SCE) was the reference electrode, (2) the graphite rod was the counter electrode and (3) the working electrode was the specimen. Each electrochemical test was rerun three times in order to ensure replicability of the results. Thereafter, the corrosion rate (R_i) and polarization resistance (R_p) of these samples were calculated according to [41, 42]:

$$R_i = 22.85 \times i_{\text{corr}} \quad (1)$$

$$R_p = \frac{\beta_a \beta_c}{2.3(\beta_a + \beta_c) i_{\text{corr}}} \quad (2)$$

where i_{corr} is the corrosion current density, β_c is the cathodic Tafel slope and β_a is the anodic Tafel slope. Eventually, the calculations of the output results were based on the polarization curves for Ti–Ta– x Sn SMAs.

The antibacterial activities with and without metal ions (Sn) were established by the agar disc diffusion technique using the bacterial species *Escherichia coli* (gram-negative

bacteria) [43]. These bacteria were obtained from the Institute of Medical Research (IMR), Kuala Lumpur. The glassware was sterilized for 20 min in an autoclave at 393 K prior to the experiment. Stock solutions for each organism were prepared by mixing 1 mL of each bacteria solution with 9 mL of Luria–Bertani (LB) broth and incubated at 310 K for 24 h with shaking at 250 rpm. For disc diffusion, solidified nutrient agar media were swabbed with respective organisms ($n = 2$) (1×10^8 CFU mL⁻¹). Four discs on each plate were fixed at equal distance and incubated at 310 K for 24 h. The experiment was repeated three times, and only one the best image was photographed with a digital camera. The mean zone of inhibition (mm) around the film was measured using ImageJ software, version 1.47.

Results and discussion

Microstructure characterization

Figure 2 displays scanning electron microscopy (SEM) micrographs of Ti–30Ta and Ti–30Ta– x Sn SMAs fabricated PM and followed by microwave sintering. These micrographs demonstrate two types of morphologies—needles like (N) and plates like (P). The plate-like morphology is predominant with a slight presence of needles-like morphology. According to energy-dispersive spectroscopy (EDS), the morphology of the surface exhibits two regions—the dark region refers to the Ti-rich region, while the bright area is related to the Ta-rich region [44–46]. The growth of the plates and the needles commences from the contact area between the two regions towards the centre of the Ti-rich region (Ti-particle) and may be because of the diffusion of Ta towards the Ti region [47], while the diffusion of Ti towards the Ta region makes it darker, especially at the edges (Ta-particle) which is in contact with the Ti-rich region [44]. The P and N morphologies are an exhibition of the β phase, but there are other β needle-like morphologies that look like spaghetti (S) or irregular lines containing the α phase between them [48–50], just as indicated in Fig. 2b and c. The grain sizes clearly increased with rising tin additions [51]. However, the porosity of these alloys decreased gradually with increasing tin additions and was in the range of 26–30%. It was reported by Terayama et al. [52] that adding elemental additions with lower melting point was so effective in increasing the density (reduce the porosity) of the sintered alloy. Figure 2e shows the EDS of Ti–30%Ta–2.26% Sn, and 1 and 2 represent the EDS points on the micrograph of Fig. 2d. The diffusion of Sn into Ti particles was greater than that of Ta particles [53, 54]. Figure 2 (1) shows the EDS point at the edge of the Ti particles, where the percentage of diffused Ta was very low (3.06 at.%), while the diffused tin

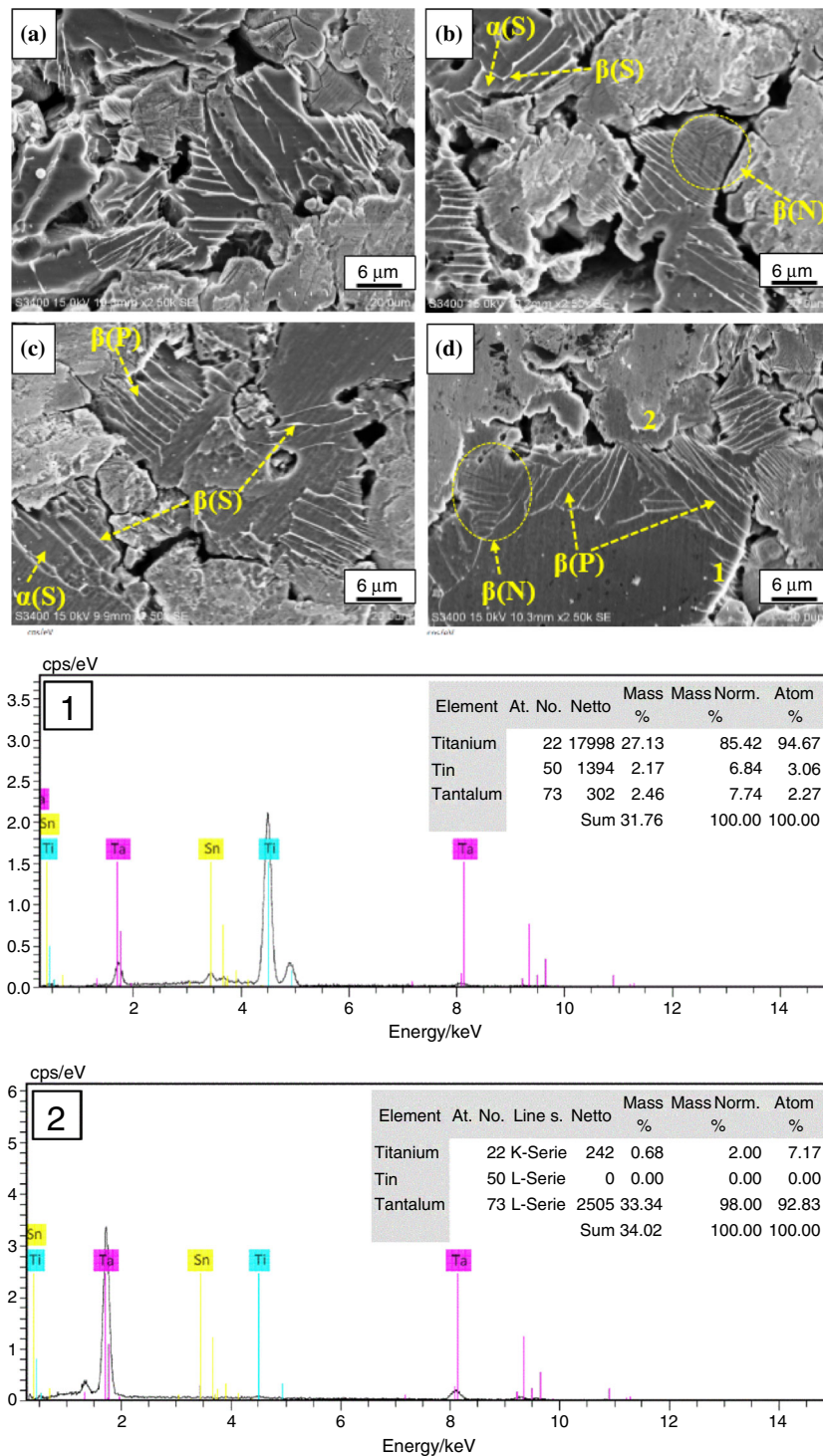


Fig. 2 SEM micrographs showing the microstructure of **a** Ti-30Ta, **b** Ti-30Ta-0.37Sn, **c** Ti-30Ta-0.745Sn, **d** Ti-30Ta-2.26Sn alloys and **e** (1 and 2) EDS of Ti-30Ta-2.26Sn

percentage was very close to the real composition of tin in the alloy (2.27 at.%). On the other hand, Fig. 2 (2) shows the EDS point at the edge of the Ta particles, where the proportion of Ta was 92.83 at.% with very minimal amounts of diffused Ti (7.17 at.%), though we could not observe any

presence of tin (oxygen was removed from the EDS setting for easier explanation of the elements' diffusion).

Figure 3 depicts the XRD patterns of Ti-30Ta and Ti-30Ta-*x*Sn that verified the phase composition in the microstructure and its effect on these SMAs. The identified

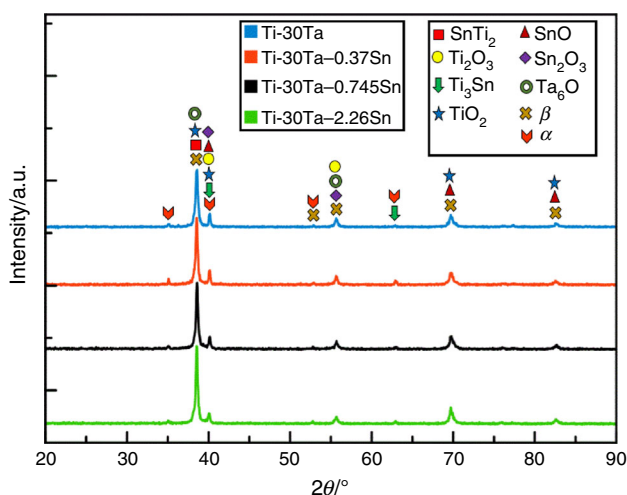


Fig. 3 XRD patterns of Ti-30Ta and Ti-30Ta-*x*Sn alloys

phases were the β -phase [body-centred cubic (BCC)] structure and α phase [close packed hexagonal (CPH)]. The β phase of Ti and Ta was the main phase that matched the (110), (200), (211) and (220) planes of angles 38.6° , 55.7° , 69.7° and 82.6° , respectively [46], while the β phase of Sn matched the 002 plane of angle 52.8° . Phase α was present at the (100), (101) and (102) planes of angles 35.17° , 40.19° and 52.8° , respectively, that represented the Ti element. The phase α (Ta) indicated at the (411) plane of angle 40.19° , and phase α (Sn) indicated at the (112) plane of angle 62.9° . The intensity of the β phase at the plane of (110) was enhanced with increasing Sn addition. SnTi_2 matched the (110) plane of the angle 38.6° , and Ti_3Sn was observed at the (201) and (220) planes of angles 40.19° and 62.9° , respectively. The XRD and EDS results demonstrated the presence of Sn in compounds with Ti and did not appear with Ta. TiO_2 presents at the (112), (022), (122) and (224) planes of angles 38.6° , 40.19° , 69.7° and 82.6° , respectively, while Ti_2O_3 was present at the (113) plane of angle 40.19° and the (122) plane of angle 55.7° . SnO was apparent at the (114), (220) and (213) planes of angles 40.19° , 69.7° and 82.6° , respectively, while Sn_2O_3 was found at the (-201) plane of angle 40.19° and the (141) plane of angle 55.7° . Ta_6O (β) was observed at the (101) plane of an angle 38.6° and the (200) plane of angle 55.7° .

Transformation temperatures

Figure 4 presents the DSC curves of Ti-Ta-*x*Sn SMAs. The transformation temperatures were austenite start and martensite start (A_s and M_s) temperatures, and austenite finish and martensite finish (A_f and M_f) temperatures were identified by the conventional employed extrapolation of temperatures of the onset and offset on the curve baseline; utilizing the extrapolating temperatures of the onset and

offset in the thermal analysis is common. The employment of deviation point from the curve baseline (onset and offset temperatures) might have been better instead of extrapolating temperatures to explain the influences in the DSC curves of diffusionless martensitic transformations. Therefore, an extrapolating value was used to satisfy the universal trend in the DSC and prevent the subjectiveness of the selection of the deviation point. Figure 4 shows that the exothermic peak appeared during the cooling process, while a multi-step phase transformation in which A_s transforms to A_f appeared during heating. The TA Instrument software indicates that the upper part from the curve is an exothermic reaction (martensitic transformation) while the lower curve is endothermic reaction (austenitic transformation). In other words, the upper part is under cooling (M_s to M_f , from the right to the left), while the lower part is under heating [A_s to A_f , from the left to the right]. The transformation peaks for both martensite and austenite transformation become more obvious as the amount of Sn increases. This is due to the formation of intermetallic compounds of Ti-Sn. Also, it was found that an increase in the relative amount of Ta in a Ti matrix results in a decrease in the martensitic transformation temperature (M_s) [28]. Based on the previous researches [55, 56], it was found that with a large amount of Sn addition, the martensitic transformation is difficult to occur in Ti alloys; furthermore, the Sn addition may have an effect on the stabilization of Ti-based alloys and thus increase the stability of β phase. Furthermore, as outlined by Gutiérrez-Moreno et al. [57] that in Ti alloy, the β phase is stable at low Sn substitutions; however, increasing Sn concentration induces instability. In other words, the small amounts of Sn affect as β -Ti stabilizers despite the fact that large amounts of Sn affect as α -Ti stabilizers. On the other hand, the transformation temperature curves for the forward and backward transformation shown few additional peaks were also being observed (see Fig. 4) and their presence is mainly related to α -precipitates/intermetallic compounds that are formed during the addition of tin [58, 59]. The reason of presence of these peaks also can be refer to the contemplation of different stress regions close to and also apart from the precipitates upon cooling; the transformation starts in the stressed area around the precipitates once the temperature occurs closer to the alloy martensitic transformation. Based on the Clausius–Clapeyron equation, the occurrence of stresses in the alloy consistently improves the martensitic transformation temperature. Once martensite forms [60], the stress field is relaxed near the precipitates and additional martensite transformation inhibited temporarily. Upon further cooling, as the temperature goes down to stress-free martensite start temperature, the martensitic transformation again starts. In this kind of transformation, the initial martensite peak

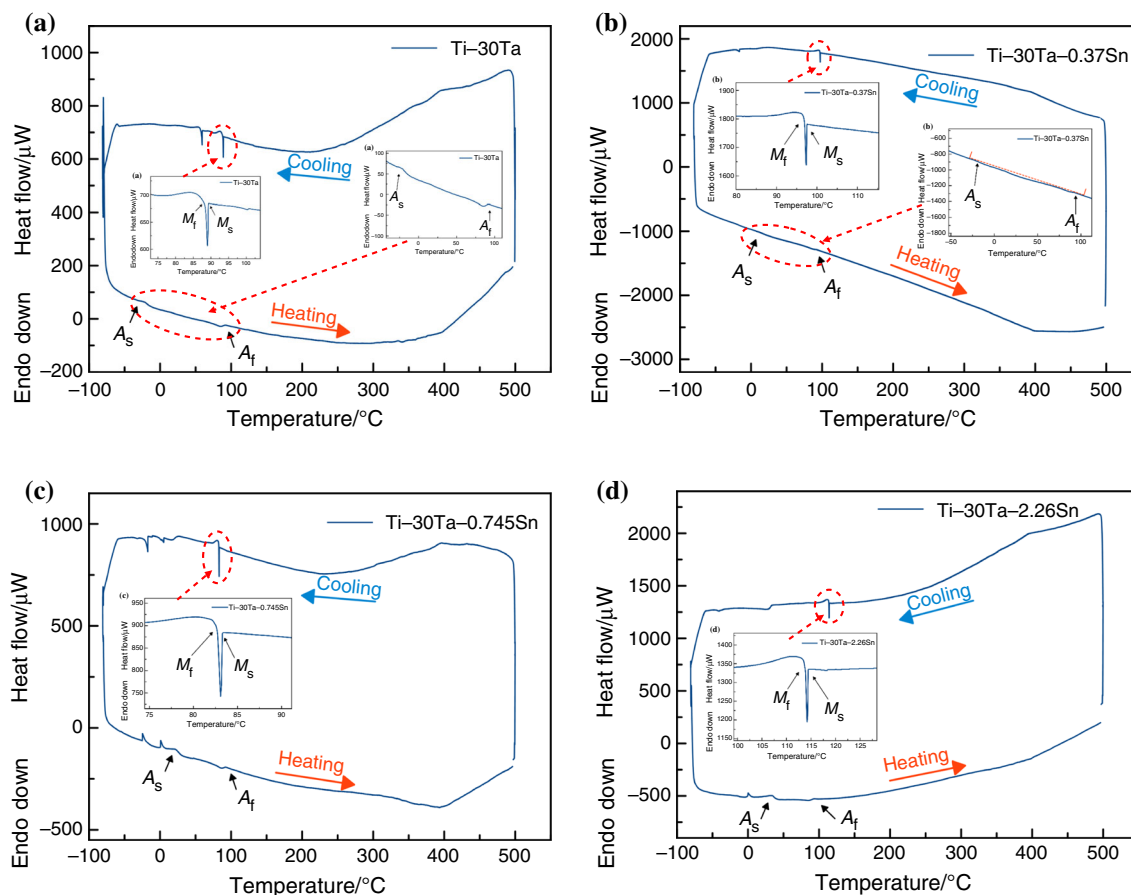


Fig. 4 DSC curves of **a** Ti-30Ta, **b** Ti-30Ta-0.37Sn, **c** Ti-30Ta-0.745Sn and **d** Ti-30Ta-2.26Sn alloys

arises with greater transformation heat released when compared with the final martensite peak [61]. According to the analysis of the transformation curves, the A_s , A_f , M_s and M_f were determined and given in Table 2. During heating, the range between A_s and A_f tended to decrease with the increased tin addition in the Ti-Ta SMA. In modified and unmodified Ti-Ta SMAs, the range of the A_s to A_f transformation was approximately 250.42 to 365.8 K, respectively, while the range of the M_s to M_f transformation range was 389.65 to 355 K, respectively. At human body temperature (310 K), the transformation to martensite was

already achieved, and this temperature was in the range of the A_s to A_f transformation for all these samples. In other words, that meant during the application of stress, these alloys became of martensitic α'' because of the transformation from the β phase to the α'' phase, bringing about improvement in shape memory behaviour [62–64]. With Ti, tin additions behave as neutral solutes and have little effect on the transformation temperature [65].

Mechanical properties

Stress–strain curves

Figure 5a, b displays the stress–strain curves of the Ti-Ta SMAs after being modified with the Sn addition. These curves can be divided into three regions [66] as portrayed in Fig. 5b. Region 1 is a linear region of elastic deformation, where the elastic modulus can be observed, followed by region 2 in which the plastic yield deformation took place, in which a compressive peak strength could have been observed. Meanwhile, region 3 was a rupture region.

Table 2 Transformation temperatures of Ti-Ta and Ti-Ta-xSn SMAs

MWS parameters	M_s /K	M_f /K	A_s /K	A_f /K
Ti-30Ta	362.26	359.48	250.42	365.11
Ti-30Ta-0.37Sn	370.7	369.16	285.57	365.13
Ti-30Ta-0.74Sn	356.5	355	293.9	365.17
Ti-30Ta-2.26Sn	389.65	386.4	307.7	365.8

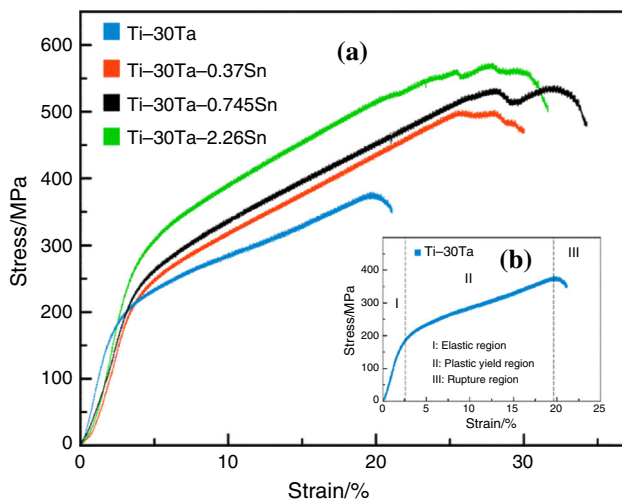


Fig. 5 **a** Compressive curves of Ti–30Ta and Ti–Ta–*x*Sn alloys and **b** illustration of the three regions of the Ti–30Ta alloy stress–strain curve

The increase in tin improved the fracture strength and strain, where the fraction strength and strain of the samples with 0, 0.37, 0.745 and 2.26 at.% Sn were 375 MPa at 19.68%, 497 MPa at 28%, 534 MPa at 32% and 570 MPa at 27.75%, respectively. The value of the elastic modulus was increased gradually with rising Sn (7.2 to 8.2 GPa), where the highest value was observed with the percentage of 2.26 at.% Sn. Based on these readings, it was indicated that the elastic modulus of these SMAs was very close to the elastic modulus of human bone (3–20 GPa for cortical bone) [67]. On the other hand, the low elastic modulus of these samples was based on the microwave sintering process solving one of the most critical problems that occurred between the elastic modulus of the hard tissue (<20 GPa) and the elastic modulus of the implant materials (>100 GPa). This large elastic modulus discrepancy is called “stress shielding”, which may lead to the resorption of hard tissue, loosening of implants and, finally, the failure of implantation [9, 68, 69]. This improvement in mechanical properties from the addition of tin and the production method means these alloys are more appropriate for biomedical applications [33, 51]. The Ti–Ta–2.26% Sn showed maximum fracture strength, while the maximum fracture strain was observed in Ti–Ta–0.745% Sn. However, the presence of porosity and low elastic modulus effects were directly related to the hardness of these alloys [70], where the Vickers hardness of the samples with 0, 0.37, 0.745 and 2.26 at.% Sn was 50, 40.5, 41.5 and 45 Hv, respectively. The Vickers hardness rose with an elevation of elastic modulus after adding Sn (still less than the base alloy). Yet, generally, the elastic modulus and Vickers hardness were low, and that may be connected to the microwave sintering method [70].

Shape memory effect

Strain recovery (ε) by the SME of the Ti–Ta SMAs with and without Sn addition was determined through a specially designed compression test at $T < M_s$ [human body temperature (310 K)]. The strain recovery by SME (ε_{SME}) changed with the changes in the amount of Sn at the strain value of 4% (see Fig. 6). It appeared that the addition of Sn at different atomic percentages yielded an increase in the value of ε_{SME} . The alloy with a 0.745 at.% Sn exhibited the highest shape recovery after the preheating process at $T > A_f$. Additionally, the strain recovery (ε) with the SME increased from 37.5 to 45%. However, there were decreases in strain recovery of the sample at 2.26 at.% Sn compared with those of 0.37 and 0.745 at.% Sn, even if the XRD exhibited little enhancement in the intensity of the β phase and minor reduction in the α phase that should have improved the strain recovery of this sample because the SME diminished when raising the precipitates of the equilibrium of the α phase [71]. However, the β phase was able to transform to martensitic α'' phase by adding stress during loading; meanwhile, during unloading with the release of the stress, the unstable martensitic α'' phase mostly transformed back to the β phase [62–64]. This decrement was mainly attributed to increasing Sn content, causing precipitation at the grain boundaries that led to a drop in strain recovery, this precipitation depending on the solubility of Sn in Ti [58, 59]. This could be observed from the TiSn phase diagram around 2.3 at.%, at a sintering temperature of 900 °C. These improvements in ε were related to the presence of SnTi_2 that appeared based on the Sn additions in the parent phase. Moreover, the percentage of ε mainly depended on the amplitude of martensitic transformation of these alloys as observed from the XRD peaks, suggesting mildly higher intensities after Sn was added. Sn appears in SnTi_2 as the main phase and Ti_3Sn precipitates.

Corrosion test

The electrochemical polarization curves of the Ti–Ta and Ti–Ta–*x*Sn SMAs in SBF solution are shown in Fig. 7. The corrosion potential (E_{corr}) of the Ti–Ta sample (–133.417 mV) shifted to the nobler direction after Sn addition (25.943 mV, at 2.26% Sn). From the i_{corr} comparison between the binary and ternary shape memory alloys, it can be inferred that the Ti–30at.% Ta SMA demonstrated the most favourable corrosion behaviour as a result of its consistently low corrosion rate in corrosive media. The Ti–Ta alloy presented the highest corrosion current density (i_{corr}) versus the alloys that included Sn addition. Table 3 lists the electrochemical parameters of the Ti–Ta and Ti–Ta–*x*Sn samples, and it is evident the

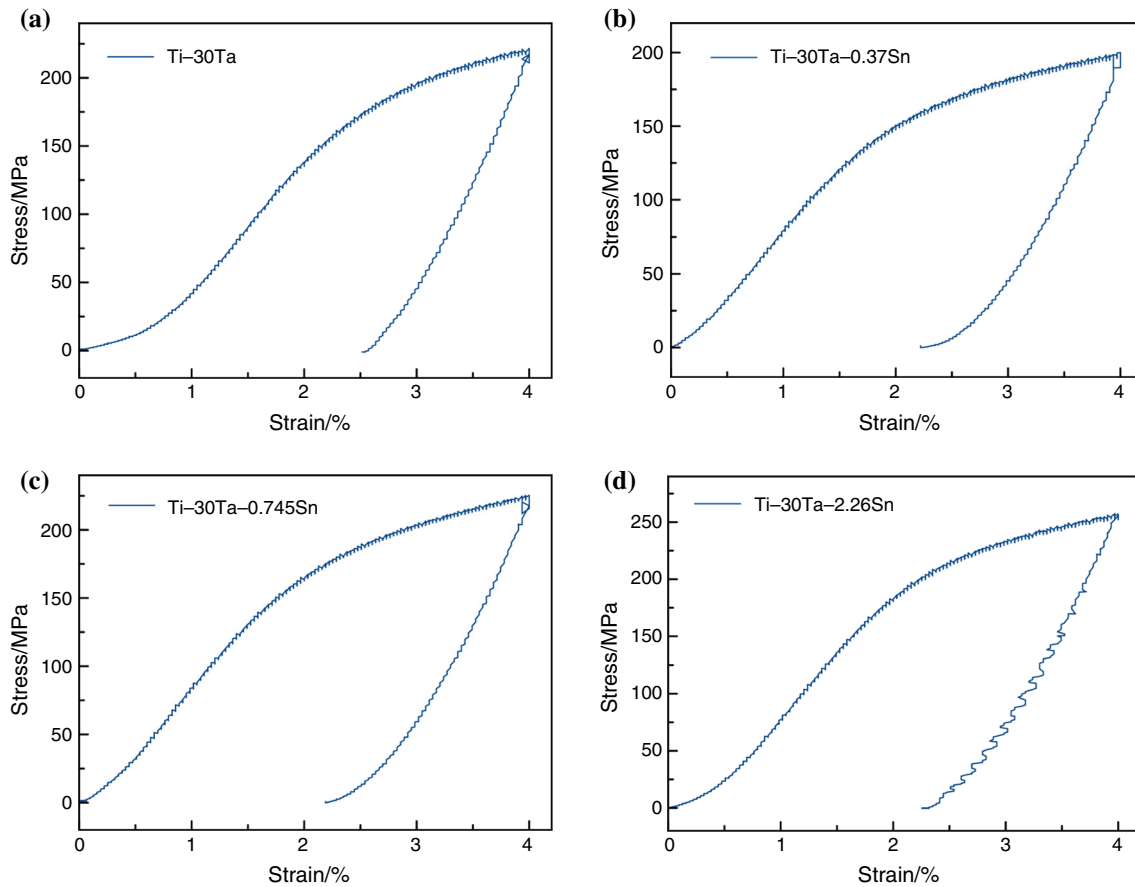


Fig. 6 The ε behaviour demonstrates the stress–strain curves of **a** Ti–30Ta, **b** Ti–30Ta–0.37Sn, **c** Ti–30Ta–0.745Sn and **d** Ti–30Ta–2.26Sn SMAs

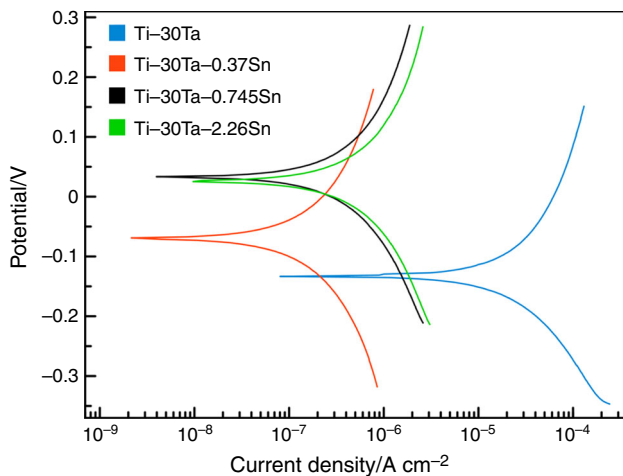


Fig. 7 Potentiodynamic polarization curves of the Ti–30Ta– x Sn SMAs

polarization resistance was enhanced after adding Sn, potentially because of the presence of Sn with the oxide layer of TiO_2 that improves the effect of this layer in an aggressive environment and hence improves corrosion resistance [72]. The Ti–30Ta–0.37Sn SMA possessed the

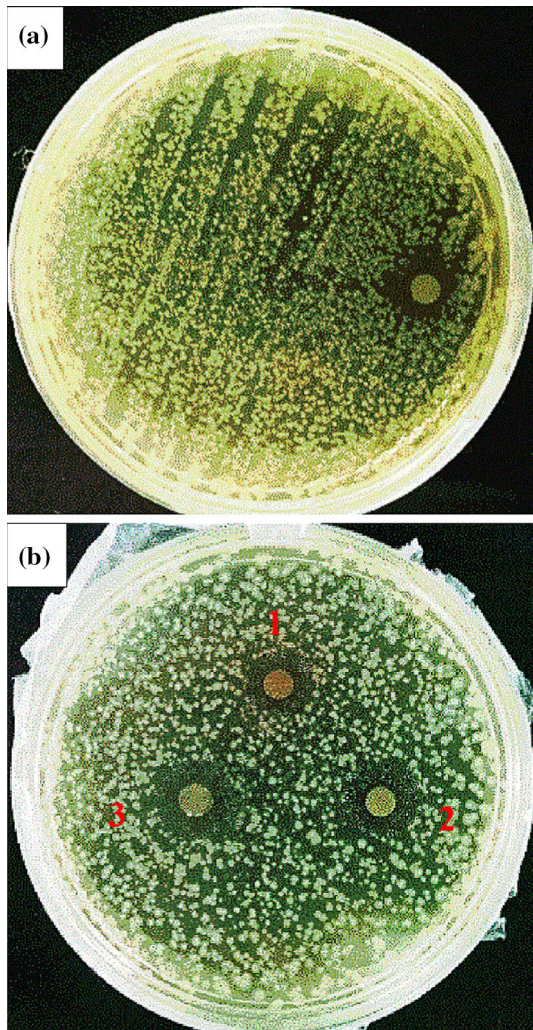
highest polarization resistance (308.44 $\text{k}\Omega$) and lowest corrosion rate ($0.0059752 \text{ mm year}^{-1}$).

Antibacterial test

The antibacterial activity results of the Ti–Ta and Ti–Ta–Sn samples against *E. coli* are shown in Fig. 8. The average of the inhibition zones for Ti–Ta was found to be 2.7 mm against *E. coli*. The average of the inhibition zones for Ti–Ta– x Sn was found to be 2.9, 3.5 and 3.8 mm against *E. coli* for 0.37, 0.745 and 2.26 at.% Sn, respectively. The antibacterial activity the Ti–Ta–Sn samples was thought to be because of the binding of the composite metals (Ti–30Ta and Ti–30Ta– x Sn) to the outer membrane of *E. coli* bacteria. It can be observed that with increasing additions of tin metal, antibacterial activity was more pronounced. The inhibition zones were larger with the rise in tin additions. Several studies have reported the antibacterial effect of tantalum and tin oxides, as these oxides exhibit robust antibacterial effects [39, 40, 73, 74]. Other investigations have also mentioned the superb antibacterial properties of TiO_2 [75–79].

Table 3 Electrochemical parameters of Ti–Ta and Ti–Ta–Sn samples in SBF solution obtained from the polarization test

Alloy	Corrosion potential, E/mV	Current density, $i_{corr}/\mu A\ cm^{-2}$	Cathodic slope, β_c/mV	Anodic slope, β_a/mV	Polarization resistance, $R_p/k\Omega$	Corrosion rate, $R_i/mm\ year^{-1}$
Ti–Ta	–133.417	34.33	246.857	393.27	2.097	0.7844405
Ti–Ta–0.37Sn	–69.794	0.2615	355.57	387.9	308.44	0.0059752
Ti–Ta–0.745Sn	32.964	0.631	324.764	394.126	122.68	0.0082488
Ti–Ta–2.26Sn	25.943	0.8005	311.316	367.531	91.54	0.0182914

**Fig. 8** Inhibition zones around the samples against *E. coli* of **a** Ti–30Ta, **b-1** Ti–30Ta–0.37Sn, **b-2** Ti–30Ta–0.745Sn and **b-3** Ti–30Ta–2.26Sn SMAs

Conclusions

This research studied the effect of Sn on the structure and properties of Ti–30at.% Ta SMAs, which resulted in a significant change in the microstructure and thus enhanced

mechanical and shape memory properties along with improving corrosion resistance and antibacterial effect. The results here revealed that the modified and unmodified Ti–30at.% Ta SMAs contained α and β phases associated with a minor presence of tin intermetallic compounds. Precipitates, in addition to the volume fraction of these phases, varied based on the change in the chemical composition of the designed alloys (depending on Sn amounts). With this in mind, it was also demonstrated that the presence of tin element with small contents has effect on porosity. It was also proposed that increasing the amount of Sn additions can lead to enhance the α -phase stability of the modified alloys. The mechanical properties of elastic modulus and strain fracture were divergent based on the variations of the α and β phases. The modified alloy with 2.26 at.% Sn showed higher strength and elastic modulus than other alloys, while the highest values for fracture strain and strain recovery by shape memory were induced with 0.745 at.% Sn addition. The modified alloys also displayed higher corrosion resistance compared with the unmodified alloys in SBF at 310 K. This can be evidenced by the lower corrosion current density, i_{corr} ($0.2615\ \mu A\ cm^{-2}$), in the PDP test. In addition, the results also showed that the modified alloys with Sn additions could enhance the antibacterial effect of Ti–Ta SMAs. Overall, our systematic method, additions, sample preparation and characterization may constitute a basis for the production of high-quality biocompatible Ti–30%Ta SMAs.

Acknowledgements The authors would like to thank the Ministry of Higher Education of Malaysia and Universiti Teknologi Malaysia for providing the financial support under the University Research Grant No. Q.J130000.3024.00M57 and research facilities.

References

1. Liu Y. The superelastic anisotropy in a NiTi shape memory alloy thin sheet. *Acta Mater.* 2015;95:411.
2. Artiaga R, García A, García L, Varela A, Mier J, Naya S, et al. DMTA study of a nickel–titanium wire. *J Therm Anal Calorim.* 2002;70(1):199–207.

3. Long M, Rack H. Titanium alloys in total joint replacement—a materials science perspective. *Biomaterials*. 1998;19(18):1621–39.
4. Huiskes R, Weinans H, Van Rietbergen B. The relationship between stress shielding and bone resorption around total hip stems and the effects of flexible materials. *Clin Orthop Relat Res*. 1992;274:124–34.
5. Lipscomb IP, Nokes LD. The application of shape memory alloys in medicine, vol. 1. New York: Wiley; 1996. p. 154. ISBN 0-85298-956-3.
6. Hosoda H, Hanada S, Inoue K, Fukui T, Mishima Y, Suzuki T. Martensite transformation temperatures and mechanical properties of ternary NiTi alloys with offstoichiometric compositions. *Intermetallics*. 1998;6(4):291–301.
7. Zlá S, Smetana B, Žaludová M, Dobrovská J, Vodárek V, Konečná K, et al. Determination of thermophysical properties of high temperature alloy IN713LC by thermal analysis. *J Therm Anal Calorim*. 2012;110(1):211–9.
8. Kapanen A, Ryhänen J, Danilov A, Tuukkanen J. Effect of nickel–titanium shape memory metal alloy on bone formation. *Biomaterials*. 2001;22(18):2475–80.
9. Geetha M, Singh A, Asokamani R, Gogia A. Ti based biomaterials, the ultimate choice for orthopaedic implants—a review. *Prog Mater Sci*. 2009;54(3):397–425.
10. Otsuka K, Ren X. Physical metallurgy of Ti–Ni-based shape memory alloys. *Prog Mater Sci*. 2005;50(5):511–678.
11. McKelvey A, Ritchie R. Fatigue-crack propagation in nitinol, a shape-memory and superelastic endovascular stent material. *J Biomed Mater Res*. 1999;47(3):301–8.
12. Li J, Yang H, Wang H, Ruan J. Low elastic modulus titanium–nickel scaffolds for bone implants. *Mater Sci Eng C*. 2014;34:110–4.
13. Wever D, Veldhuizen A, De Vries J, Busscher H, Uges D, Van Horn J. Electrochemical and surface characterization of a nickel–titanium alloy. *Biomaterials*. 1998;19(7):761–9.
14. Plant SD, Grant DM, Leach L. Behaviour of human endothelial cells on surface modified NiTi alloy. *Biomaterials*. 2005;26(26):5359–67.
15. Mockers O, Deroze D, Camps J. Cytotoxicity of orthodontic bands, brackets and archwires in vitro. *Dent Mater*. 2002;18(4):311–7.
16. Ryhänen J, Kallioinen M, Tuukkanen J, Junila J, Niemelä E, Sandvik P, et al. In vivo biocompatibility evaluation of nickel–titanium shape memory metal alloy: muscle and perineural tissue responses and capsule membrane thickness. *J Biomed Mater Res*. 1998;41(3):481–8.
17. Duerig T, Pelton A, Stöckel D. An overview of nitinol medical applications. *Mater Sci Eng A*. 1999;273:149–60.
18. Miyazaki S, Kim H, Hosoda H. Development and characterization of Ni-free Ti-base shape memory and superelastic alloys. *Mater Sci Eng A*. 2006;438:18–24.
19. Wever D, Veldhuizen A, Sanders M, Schakenraad J, Van Horn J. Cytotoxic, allergic and genotoxic activity of a nickel–titanium alloy. *Biomaterials*. 1997;18(16):1115–20.
20. Niinomi M. Fatigue performance and cyto-toxicity of low rigidity titanium alloy, Ti–29Nb–13Ta–4.6Zr. *Biomaterials*. 2003;24(16):2673–83.
21. Laheurte P, Prima F, Eberhardt A, Gloriant T, Wary M, Patoor E. Mechanical properties of low modulus β titanium alloys designed from the electronic approach. *J Mech Behav Biomed Mater*. 2010;3(8):565–73.
22. Ning C-Q, Zhou Y. Development and research status of biomedical titanium alloys. *Cailiao Kexue yu Gongyi/Mater Sci Technol*. 2002;10(1):100–6.
23. Fukui Y, Inamura T, Hosoda H, Wakashima K, Miyazaki S. Mechanical properties of a Ti–Nb–Al shape memory alloy. *Mater Trans*. 2004;45(4):1077–82.
24. Kim HY, Hashimoto S, Kim JI, Hosoda H, Miyazaki S. Mechanical properties and shape memory behavior of Ti–Nb alloys. *Mater Trans*. 2004;45(7):2443–8.
25. Kim HY, Ohmatsu Y, Kim JI, Hosoda H, Miyazaki S. Mechanical properties and shape memory behavior of Ti–Mo–Ga alloys. *Mater Trans*. 2004;45(4):1090–5.
26. Maeshima T, Nishida M. Shape Memory properties of biomedical Ti–Mo–Ag and Ti–Mo–Sn alloys. *Mater Trans*. 2004;45(4):1096–100.
27. Duerig T, Albrecht J, Richter D, Fischer P. Formation and reversion of stress induced martensite in Ti–10V–2Fe–3Al. *Acta Metall*. 1982;30(12):2161–72.
28. Buenconsejo PJS, Kim HY, Hosoda H, Miyazaki S. Shape memory behavior of Ti–Ta and its potential as a high-temperature shape memory alloy. *Acta Mater*. 2009;57(4):1068–77.
29. S-Y Yang, W-J Jin, Y-N Wang, C-P Wang, X-J Liu. Microstructure, mechanical and shape memory properties of Ti–55Ta–xSi biomedical alloys. *Trans Nonferr Met Soc China*. 2011;21(2):287–91.
30. Zhou YL, Niinomi M, Akahori T. Effects of Ta content on Young's modulus and tensile properties of binary Ti–Ta alloys for biomedical applications. *Mater Sci Eng A*. 2004;371(1):283–90.
31. Sumner D, Turner T, Igloria R, Urban R, Galante J. Functional adaptation and ingrowth of bone vary as a function of hip implant stiffness. *J Biomech*. 1998;31(10):909–17.
32. Mareci D, Chelariu R, Gordin D-M, Ungureanu G, Gloriant T. Comparative corrosion study of Ti–Ta alloys for dental applications. *Acta Biomater*. 2009;5(9):3625–39.
33. Kim HY, Fukushima T, Buenconsejo PJS, Nam T-H, Miyazaki S. Martensitic transformation and shape memory properties of Ti–Ta–Sn high temperature shape memory alloys. *Mater Sci Eng A*. 2011;528(24):7238–46.
34. Ikeda M, Komatsu S-Y, Nakamura Y. Effects of Sn and Zr additions on phase constitution and aging behavior of Ti–50 mass% Ta alloys quenched from β single phase region. *Mater Trans*. 2004;45(4):1106–12.
35. Buenconsejo PJS, Kim HY, Miyazaki S. Effect of ternary alloying elements on the shape memory behavior of Ti–Ta alloys. *Acta Mater*. 2009;57(8):2509–15.
36. Buenconsejo PJS, Kim HY, Miyazaki S. Novel β -TiTaAl alloys with excellent cold workability and a stable high-temperature shape memory effect. *Scripta Mater*. 2011;64(12):1114–7.
37. Guo B, Tong Y, Chen F, Zheng Y, Li L, Chung CY. Effect of Sn addition on the corrosion behavior of Ti–Ta alloy. *Mater Corros*. 2012;63(3):259–63.
38. Khan W, Deen K, Ghauri K, Ahmad R, Tabish T, Atiq S, et al. Corrosion behaviour of Ti–Ta–Sn alloy systems in 0.9% NaCl solution. *Mater Corros*. 2012;63(11):992–6.
39. Kamaraj P, Vennila R, Arthanareeswari M, Devikala S. Biological activities of tin oxide nanoparticles synthesized using plant extract. *Pharm Pharma Sci*. 2014;3:382.
40. Amininezhad SM, Rezvani A, Amouheidari M, Amininejad SM, Rakhshani S. The antibacterial activity of SnO₂ nanoparticles against *Escherichia coli* and *Staphylococcus aureus*. *Zahedan J Res Med Sci*. 2015;17(9):1.
41. Bakhsheshi-Rad H, Idris M, Abdul-Kadir M, Ourdjini A, Medraj M, Daroonparvar M, et al. Mechanical and bio-corrosion properties of quaternary Mg–Ca–Mn–Zn alloys compared with binary Mg–Ca alloys. *Mater Des*. 2014;53:283–92.
42. Argade G, Kandasamy K, Panigrahi S, Mishra R. Corrosion behavior of a friction stir processed rare-earth added magnesium alloy. *Corros Sci*. 2012;58:321–6.
43. Iqbal N, Kadir MRA, Mahmood NHB, Iqbal S, Almasi D, Naghizadeh F, et al. Characterization and biological evaluation of silver containing fluoroapatite nanoparticles prepared through microwave synthesis. *Ceram Int*. 2015;41(5):6470–7.

44. Naidoo M, Raethel J, Sigalas I, Herrmann M. Preparation of (Ti, Ta)-(C, N) by mechanical alloying. *Int J Refract Metals Hard Mater.* 2012;35:178–84.
45. Naidoo M, Johnson O, Sigalas I, Herrmann M. Preparation of Ti-Ta-(C, N) by mechanical alloying Ti (C, N) and TaC. *Int J Refract Metals Hard Mater.* 2013;37:67–72.
46. Liu Y, Li K, Wu H, Song M, Wang W, Li N, et al. Synthesis of Ti-Ta alloys with dual structure by incomplete diffusion between elemental powders. *J Mech Behav Biomed Mater.* 2015;51:302–12.
47. Pineau S, Veyrac M, Hourcade M, Hocheid B. The investigation and production of titanium-tantalum junctions diffusion bonded at high temperature (855 °C to 920 °C): the influence of temperature, time pressure and roughness on the mechanical properties, and the optimisation of the bonded conditions: DTIC document. 1990.
48. de Souza KA, Robin A. Preparation and characterization of Ti-Ta alloys for application in corrosive media. *Mater Lett.* 2003;57(20):3010–6.
49. Hon Y-H, Wang J-Y, Pan Y-N. Composition/phase structure and properties of titanium-niobium alloys. *Mater Trans.* 2003;44(11):2384–90.
50. Han M-K, Kim J-Y, Hwang M-J, Song H-J, Park Y-J. Effect of Nb on the microstructure, mechanical properties, corrosion behavior, and cytotoxicity of Ti-Nb alloys. *Materials.* 2015;8(9):5986–6003.
51. Tong Y, Guo B, Zheng Y, Chung CY, Ma LW. Effects of Sn and Zr on the microstructure and mechanical properties of Ti-Ta-based shape memory alloys. *J Mater Eng Perform.* 2011;20(4–5):762–6.
52. Terayama A, Fuyama N, Yamashita Y, Ishizaki I, Kyogoku H. Fabrication of Ti-Nb alloys by powder metallurgy process and their shape memory characteristics. *J Alloy Compd.* 2013;577:S408–12.
53. Mehrer H. Diffusion in solids: fundamentals, methods, materials, diffusion-controlled processes. Berlin: Springer; 2007.
54. Ivasishin OM, Eylon D, Bondarchuk V, Savvakina DG, editors. Diffusion during powder metallurgy synthesis of titanium alloys. Defect and diffusion forum. Zurich: Trans Tech Publ; 2008.
55. Ozaki T, Matsumoto H, Watanabe S, Hanada S. Beta Ti alloys with low Young's modulus. *Mater Trans.* 2004;45(8):2776–9.
56. Hu Q-M, Li S-J, Hao Y-L, Yang R, Johansson B, Vitos L. Phase stability and elastic modulus of Ti alloys containing Nb, Zr, and/or Sn from first-principles calculations. *Appl Phys Lett.* 2008;93(12):121902.
57. Gutiérrez-Moreno J, Guo Y, Georgarakis K, Yavari A, Evangelakis G, Lekka CE. The role of Sn doping in the β -type Ti-25 at%Nb alloys: experiment and ab initio calculations. *J Alloy Compd.* 2014;615:S676–9.
58. Vellios N, Tsakirooulos P. The role of Sn and Ti additions in the microstructure of Nb-18Si base alloys. *Intermetallics.* 2007;15(12):1518–28.
59. Gorna I, Bulanova M, Valuiska K, Bega M, Koval OY, Kotko A, et al. Alloys of the Ti-Si-Sn system (titanium corner): phase equilibria, structure, and mechanical properties. *Powder Metall Met Ceram.* 2011;50(7–8):452–61.
60. Kato M, Pak HR. Thermodynamics of stress-induced first-order phase transformations in solids. *Phys Status Solidi (b).* 1984;123(2):415–24.
61. Sasaki TT, Hornbuckle BC, Noebe RD, Bigelow GS, Weaver ML, Thompson GB. Effect of aging on microstructure and shape memory properties of a Ni-48Ti-25Pd (At. Pct) alloy. *Metall Mater Trans A.* 2013;44(3):1388–400.
62. Lagoudas D. Shape memory alloys: modeling and engineering application. College Station: Springer; 2008.
63. Ehtemam-Haghighi S, Liu Y, Cao G, Zhang L-C. Influence of Nb on the $\beta \rightarrow \alpha$ martensitic phase transformation and properties of the newly designed Ti-Fe-Nb alloys. *Mater Sci Eng C.* 2016;60:503–10.
64. Kolli RP, Joost WJ, Ankem S. Phase stability and stress-induced transformations in beta titanium alloys. *JOM.* 2015;67(6):1273–80.
65. Vasudevan D, Balashanmugam P, Balasubramanian G. A study on compressive behaviour of thermal cycled titanium alloy [Ti-6Al-4V]. 2015;2(7):167–154.
66. Gao Z, Li Q, He F, Huang Y, Wan Y. Mechanical modulation and bioactive surface modification of porous Ti-10Mo alloy for bone implants. *Mater Des.* 2012;42:13–20.
67. Hench LL. Bioceramics. *J Am Ceram Soc.* 1998;81(7):1705–28.
68. Nagels J, Stokdijk M, Rozing PM. Stress shielding and bone resorption in shoulder arthroplasty. *J Shoulder Elb Surg.* 2003;12(1):35–9.
69. Niinomi M. Metallic biomaterials. *J Artif Organs.* 2008;11(3):105–10.
70. Xu J, Bao L, Liu A, Jin X, Tong Y, Luo J, et al. Microstructure, mechanical properties and superelasticity of biomedical porous NiTi alloy prepared by microwave sintering. *Mater Sci Eng C.* 2015;46:387–93.
71. Guo Y. beta-bcc and amorphous Ti-based biocompatible alloys for human body implants. Université Grenoble Alpes. 2014.
72. Khalifa O, Wahab E, Tilp A. The effect of Sn and TiO₂ nano particles added in Electroless Ni-P plating solution on the properties of composite coatings. *Aust J Basic Appl Sci.* 2011;5(6):136–44.
73. Chang Y-Y, Huang H-L, Chen H-J, Lai C-H, Wen C-Y. Antibacterial properties and cytocompatibility of tantalum oxide coatings. *Surf Coat Technol.* 2014;259:193–8.
74. Ghoranneviss M, Shahidi S. Effect of various metallic salts on antibacterial activity and physical properties of cotton fabrics. *J Ind Text.* 2013;42(3):193–203.
75. Kubacka A, Diez MS, Rojo D, Bargiela R, Ciordia S, Zapico I et al. Understanding the antimicrobial mechanism of TiO₂-based nanocomposite films in a pathogenic bacterium. *Scientific reports.* 2014;4.
76. Lu Y, Hao L, Hirakawa Y, Sato H. Antibacterial activity of TiO₂/Ti composite photocatalyst films treated by ultrasonic cleaning. *Adv Mater Phys Chem.* 2013;2(04):9.
77. Xing Y, Li X, Zhang L, Xu Q, Che Z, Li W, et al. Effect of TiO₂ nanoparticles on the antibacterial and physical properties of polyethylene-based film. *Prog Org Coat.* 2012;73(2):219–24.
78. Kim YS, Park ES, Chin S, Bae G-N, Jurng J. Antibacterial performance of TiO₂ ultrafine nanopowder synthesized by a chemical vapor condensation method: effect of synthesis temperature and precursor vapor concentration. *Powder Technol.* 2012;215:195–9.
79. Ahmad R, Sardar M. TiO₂ nanoparticles as an antibacterial agents against *E. coli*. *Int J Innov Res Sci Eng Technol.* 2013;2:3569–74.